Journal of Colloid and Interface Science 562 (2020) 112–124

Contents lists available at ScienceDirect

Journal of Colloid and Interface Science

journal homepage: www.elsevier.com/locate/jcis

Lead bismuth oxybromide/graphene oxide: Synthesis, characterization, and photocatalytic activity for removal of carbon dioxide, crystal violet dye, and 2-hydroxybenzoic acid

Fu-Yu Liu [a], Yong-Ming Dai [b], Fu-Hsuan Chen [c], Chiing-Chang Chen [a,*]

[a] Department of Science Education and Application, National Taichung University of Education, Taichung 40306, Taiwan, ROC
[b] Department of Chemical and Materials Engineering, National Chin-Yi University of Technology, Taichung 411, Taiwan, ROC
[c] Department of Political Science, National Taiwan University, Taipei 106, Taiwan, ROC

GRAPHICAL ABSTRACT

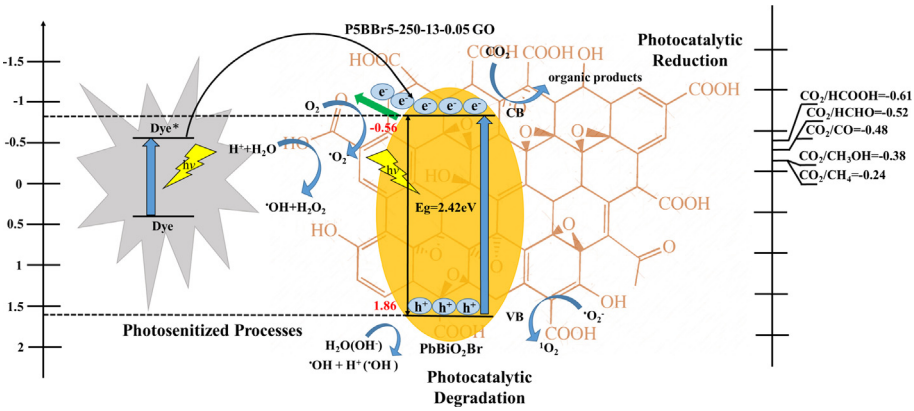

ARTICLE INFO

Article history:
Received 7 October 2019
Revised 1 December 2019
Accepted 2 December 2019
Available online 6 December 2019

Keywords:
$PbBiO_2Br$
Graphene oxide
Heterojunction
Photocatalytic
Crystal violet
2-hydroxybenzoic acid
CO_2

ABSTRACT

A novel lead bismuth oxybromide/graphene oxide ($PbBiO_2Br$/GO) composite photocatalyst were prepared using a controlled and nontemplate hydrothermal technique with $PbBiO_2Br$ and GO as the starting material. The heterojunction photocatalysts were characterized through XRD, FE-SEM-EDS, HR-TEM, XPS, DR-UV–vis, BET, PL, EPR, and UPS. Under the optimal synthesis conditions, the photocatalytic activity of $PbBiO_2Br$/GO composites was much higher than that of $PbBiO_2Br$. Under 25 °C, 1 atm, and 432-nm visible light irradiation at, the optimized $PbBiO_2Br$/GO increased the rate (at 1.913 μmol g^{-1} h^{-1}) of photocatalytic conversion from carbon dioxide (CO_2) to methane (CH_4). This conversion rate was higher than that of the original $PbBiO_2Br$ material (0.957 μmol g^{-1} h^{-1}). Therefore, $PbBiO_2Br$/GO is superior for CH_4 production and has great potential as CO_2 photoreduction catalysts. In addition, such catalytic performance (when using 0.05 wt%-GO/$PbBiO_2Br$ composite as a photocatalyst) indicates that the optimal reaction rate constants of crystal violet (CV) and 2-hydroxybenzoic acid (2-HBA) are 0.1278 and 0.0093 h^{-1}, respectively, which are 1.82 and 1.24 times the reaction rate constant of $PbBiO_2Br$ as a photocatalyst, respectively. Our findings are useful for $PbBiO_2Br$/GO synthesis and in its future environmental applications, particularly in solar fuel manufacture.

© 2019 Elsevier Inc. All rights reserved.

* Corresponding author.
E-mail address: ccchen@mail.ntcu.edu.tw (C.-C. Chen).

https://doi.org/10.1016/j.jcis.2019.12.006
0021-9797/© 2019 Elsevier Inc. All rights reserved.

1. Introduction

The increase in atmospheric carbon dioxide concentration is considered a major factor in global warming. The use of sunlight to irradiate carbon dioxide to produce hydrocarbon fuels is an important strategy for reducing the concentration of atmospheric carbon dioxide levels [1]. To reduce the toxic effects of chemicals, the removal of harmful chemicals in environmental wastewater has become one of the most important factors in contemporary pollution control methods [2]. In the growing crisis of environmental pollution and energy shortages, photocatalysis can play an important role in pollutant degradation and solar energy conversion. The photocatalytic degradation of organic pollutants can be applied to the photocatalytic reduction of carbon dioxide (CO_2) and nitrogen (N_2) to form various organic substances and promote the carbon and nitrogen cycles for sustainable development [3,4]. For practical applications of photocatalysis, photocatalysts must be highly efficient, environmentally friendly, inexpensive, and easy to recycle [5].

The elimination of toxic chemicals from wastewater has become one of the most critical aspects of modern pollution control methods, because these chemicals have harmful effects on biology and the environment. Every year around 10^6 tons and more than 10,000 different synthetic dyes and pigments are produced worldwide, and these dyes and pigments are widely used in the dye and printing industry. It is estimated that about 10% of industrial wastewater is lost. In particular, triphenylmethane (TPM) dyes are widely used as coloring agents in the leather, cosmetics, paper and food industries, for plastics, greases, waxes and varnishes [6]. Due to the potential applications of these dyes in photodynamic processing, the photocytotoxicity of TPM caused by the production of reactive oxygen species has been studied intensively. However, the oxidation of TPM in living organisms catalyzed by thyroid peroxidase has attracted much attention, because the oxidation reaction produces various *N*-dealkylated aromatic amines, which have structures similar to carcinogenic aromatic amines [7]. Recent reports indicate that TPM can act as a targeted sensitizer in the photodegradation of specific cells or cellular components [7].

The ecological survival process of many plants involves 2-salicylic acid or 2-hydroxybenzoic acid (2-HBA), a plant hormone that is used worldwide in aspirin and various foods, cosmetics, medicines and dermatological products, and may harm the environment. 2-HBA concentrations have been detected in municipal wastewater, rivers and wastewater at 50 ppm [8]. Wastewater treatment often does not eliminate 2-HBA. Even before aspirin was commercialized as an analgesic and anti-inflammatory product, doctors used plants rich in mono-HBA and its metabolic precursors for preventing and treating various chronic diseases. Pharmacologists have studied 2-HBA and recognized that aspirin and other 2-HBA-derived products can be used to prevent and treat a variety of metabolic disorders [9]. 2-HBA is a biologically active ingredient of several traditional medicines [10]. Many plants containing 2-HBA are adaptive. In other words, these plants seem to have increased stress resistance [11].

Bi-based compounds [12] such as BiOX [13,14], BiOX/BiOY [15,16], BiOX/BiOY/BiOZ (X, Y, Z = F, Cl, Br, I) [17,18], $Bi_4Ti_3O_{12}$ [19], and $BiVO_4$ [20] have been widely studied because their unique layered structures and high photocatalytic activity. The use of bismuth oxyhalides has also been highly emphasized, and these may become the third-generation solar-cell materials [21]. The Bi 6s and O 2p orbital domains can form many dispersed hybrid valence bands that facilitate the migration and oxidation reaction of photogenerated holes, thus inducing an efficient separation of photogenerated electron–hole pairs and improving the photocatalytic efficiency [22]. In recent decades, BiOX (X = F, Cl, Br, I) nanophotocatalysts have attracted considerable attention because they are economical, efficient, nontoxic, and environmentally friendly. Therefore, BiOX photocatalysts are suitable for energy conversion and environmental management. BiOX nanomaterials have unique physicochemical properties, particularly those pertaining to their layered structure as well as band structure and level. The nanostructure of BiOX can promote visible light–driven photocatalytic activity [23].

Many inorganic materials have a modular structure in which each unit is responsible for different functions. In particular, the synthesis and properties of 2D BiOX and perovskite-like bismuth oxyhalide ($PbBiO_2X$) have attracted considerable scholarly attention [18,24,25]. Recently, a new layered material ($PbBiO_2X$, X = Cl, Br, I) has attracted much attention as a photocatalysis and has been applied to organic synthesis and environmental remediation under visible light irradiation. $[Bi_2O_2]^{2+}$ slabs with the α-PbO type structure, a $[PbBiO_2]^+$ layer, and simple halide layers are effective spacers in some layered functional materials [26]. It belongs to these bismuth-based layered structure materials of the Aurivillius family with the main group, multimetal oxyhalides V-VI-VII, exhibiting covalent metal oxygen layers of $[PbBiO_2]^+$ separated by halide layers along the (0 0 1) direction [25,27].

Studies have focused on the electronic properties that cause variations in the photocatalytic activities of layered $PbBiO_2X$ materials. (X = Cl, Br, I) [27–29]. However, crystallographic parameters should also be considered to account for the photocatalytic properties of this class of compounds. Differences in the photocatalytic activities of multimetal oxyhalides are attributable to their crystal structure, optic, and redox properties [30]. The band gaps of $PbBiO_2Cl$ [29], $PbBiO_2Br$ [28,31], and $PbBiO_2I$ [32] are 2.39, 2.47, and 2.53 eV, respectively. The gaps of all of these semiconductors seem to be in the visible range to catalyze the photocatalytic reaction. Thus far, $PbBiO_2X$ composites, such as $PbBiO_2Cl$/BiOCl [25], $PbBiO_2Br$/BiOBr [28], $PbBiO_2I$/PbO [27], $PbBiO_2Br$/PbO/g-C_3N_4 [33], $PbBiO_2I$/Bi_5O_7I/g-C_3N_4 [24], Ag_3PO_4/$PbBiO_2Br$ [31], and carbonized polymer dot (CPD)/$PbBiO_2Br$ [34], have been reported to have enhanced photocatalytic efficiency. To promote sustainable development, the principle of photocatalytic degradation of organic pollutants can be used for the photocatalytic reduction of CO_2 to form organic compounds and undego the carbon cycle [34,35].

To the best of our knowledge, $PbBiO_2Br$/GO-composite semiconductors have not been reported in the literature. This is the first report of the preparation of $PbBiO_2Br$/GO composites by a template-free hydrothermal method. $PbBiO_2X$ photocatalysts can reduce CO_2 with a 2.31–2.35-eV band gap, 1.58–1.97-eV valence band, and −0.48 to −0.58-eV conduction band [28–30,32]. The double-bond resonance structure of GO can conduct photogenerated electrons and suppress the electron–hole recombination of photocatalysts. Therefore, the $PbBiO_2X$/GO-composite material can considerably enhance the photocatalytic efficiency by suppressing electron–hole recombination. Under visible light irradiation, the photocatalytic activity of $PbBiO_2Br$/GO composites was further discussed by degrading crystal violet (CV) and 2-hydroxybenzoic acid (2-HBA) and reducing the CO_2 in aqueous solution.

2. Experimental details

2.1. Materials

All reagent-grade chemicals were used without further purification. $Pb(NO_3)_2{\cdot}H_2O$ and ammonium oxalate were purchased from Osaka Chemical. 2-HBA (i.e., salicylic acid) and $Bi(NO_3)_3{\cdot}5H_2O$ were purchased from Katayama. Other reagents and CV were purchased

from TCI and p-benzoquinone from Alfa aesar. Sodium azide was purchased from Sigma-Aldrich and isopropanol from Merck. Reagent-grade HNO_3, NaOH, and CH_3COONH_4 and HPLC-grade methanol were obtained from Merck.

2.2. Instruments and analytical methods

The HPLC-MS system comprised a Waters 1525 binary pump, a 2998 photodiode array detector, and a 717 plus autosampler. A ZQ-2000 micro-mass detector and an Atlantis dC18 column (250 mm × 4.6 mm i.d., d_p = 5 μm) were used for separation and identification. The column effluent was introduced into the ESI source of the mass spectrometer. Field-emission (FE) scanning electron microscopy (SEM)–energy-dispersive X-ray spectroscopy (EDS) measurements were performed on HITACHI SU-1510 and JEOL JSM-7401F (acceleration voltage = 30 and 15 kV, respectively). The FE transmission electron microscopy (TEM) images, selected area electron diffraction patterns, high-resolution (HR) TEM images, and EDS were obtained using JEOL-2010 (accelerating voltage = 200 kV). X-ray diffraction (XRD) patterns were recorded on a Rigaku SmartLab-3 equipped with Cu-Kα radiation, operating at 60 kV and 60 mA. Al-Kα radiation was generated at 15 kV. HR X-ray photoelectron spectroscopy (XPS) measurements were conducted on PHI Quantera II. The Brunauer–Emmett–Teller (BET) specific surface areas (S_{BET}) of the samples were measured on an automated system (Micrometrics Gemini VII) with N_2 gas as the adsorbate at liquid nitrogen temperature. Ultraviolet photoelectron spectroscopy (UPS) measurements were performed using ULVAC-PHI XPS and PHI Quantera SXM.

2.3. $PbBiO_2Br$/GO synthesis

The synthesis method of $PbBiO_2Br$ has been detailed in the literature [28,33]. The $PbBiO_2Br$/GO composite was produced using a controllable hydrothermal process. First, Solutions A and B were prepared as follows:

Solution A: (1) add 5 mmol of $Bi(NO_3)_3{\cdot}5H_2O$ was added to a 100-mL beaker and (2) mix it with 5 mL of deionized water under continuous stirring.

Solution B: (1) add × g of GO was first to a 100-mL beaker and (2) mixed it with 10 mL of deionized water under ultrasonic oscillation.

Solution A was then added to Solution B, followed by the addition of 5 mmol of 1 M $Pb(NO_3)_2{\cdot}H_2O$ and stirring. Under continuous stirring, 5 M NaOH was added dropwise to adjust the mixture to pH = 13. Subsequently, when a white precipitate formed, 1 or 3 mL of 5 M KBr was added dropwise. The suspension was then stirred vigorously for 30 min. Next, 24 mL of the colloidal solution was transferred to a 30-mL Teflon-lined autoclave, which was heated to 200 °C or 250 °C for 12 h, and then naturally cooled to room temperature. These obtained solid crystals were collected through filtration, washed with deionized water and ethanol to remove any possible ionic substances in the solid crystals, and finally, dried at 60 °C overnight. Depending on the obtained Pb $(NO_3)_2{\cdot}H_2O$/KBr molar ratio of 5:5 (or 5:15), pH of 13, temperature of 200 °C (or 250 °C), and hydrothermal reaction time of 12 h, the prepared sample was labeled from P5BBr5-250-13 (or P5BBr15-200–13) to P5BBr5-250-13-0.1 g GO (or P5BI15-200-13-0.1 g GO), as detailed in Table 1.

2.4. Photocatalytic reaction

2.4.1. Photocatalytic reduction of CO_2

First, 0.5 g of the photocatalyst and 300 mL of a 1 N aqueous NaOH solution were added to the quartz glass reactor. High-purity Ar was then purged into the quartz reactor. Subsequently, high-purity CO_2 was introduced into the reactor that contained the alkaline solution. Eight xenon (Xe) lamps (8 W, Philips T5) were used as a light source around the reactor to initiate a photocatalytic reaction. The photocatalytic reaction temperature was maintained at room temperature. During each reaction, after appropriate sampling, the sample was injected into a gas chromatograph (Thermo-Fisher, TRACE 1300) equipped with an FID detector and a capillary column (HP-PLOT/Q) to analyze the gas product.

2.4.2. Photocatalytic degradation of CV (or 2-HBA)

Photocatalytic experiments were performed in a 100-mL Pyrex flask containing 100 mL of 10 ppm aqueous CV (or 2-HBA) solution. The 10-mg composite photocatalyst powder was added to this flask. The pH of the suspension was adjusted by adding either NaOH or HNO_3 solution. Dark experiments were performed to examine the adsorption–desorption equilibrium. The solution was continuously stirred for 30 min to reach the adsorption–desorption equilibrium and photocatalytic reaction was then performed under visible light irradiation.

The photocatalyst (10 mg) was mixed with 100 mL of aqueous CV solution of a known initial concentration in a 100-mL flask and the mixture was shaken in an orbital shaker at 100 rpm at a constant temperature. Before the irradiation, the suspension was magnetically stirred in dark for approximately 30 min to establish an adsorption–desorption equilibrium between the CV and catalyst surface. Irradiation was performed using 150-W Xe arc lamps; the light intensity was fixed at 31.2 W/m^2, and the reaction vessel was placed 30 cm away from the light source. At given irradiation time intervals, a 5-mL aliquot was collected and centrifuged to remove the catalyst.

2.4.3. Evaluation of the effect of the active species

In the photocatalytic process, the reactive oxygen species, i.e., superoxide anion radical ($O_2^{-\cdot}$), singlet oxygen ($^1O_2$), hydrogen peroxide (H_2O_2), hole (h^+), and hydroxyl radical ($^{\cdot}OH$), has been fully investigated with regard to its detection method and production mechanism [36]. Different quenchers have been introduced to remove the relevant active substances to evaluate the role of the active substances in the photocatalytic reaction process. The active species, $^{\cdot}OH$, $O_2^{\cdot-}$, h^+, and $^1O_2$, were studied by adding 1.0 mM isopropanol (IPA, a quencher of $^{\cdot}OH$) [37], 1.0 mM benzoquinone (BQ, a quencher of $O_2^{\cdot-}$) [38], 1.0 mM ammonium oxalate (AO, a quencher of h^+) [39], and 1.0 mM sodium azide (SA, a quencher of $^1O_2$ [40], respectively.

Table 1
Codes of as-prepared samples under different hydrothermal conditions. (Pb:Br = 5:5, [Bi^{3+}] = 5 mmol, pH = 13, temp = 250 °C, time = 12 h).

Temperature (°C)	GO weight (g)			
	0.005 g	0.025 g	0.05 g	0.1 g
250	P5BBr5-250-13-0.005 g	P5BBr5-250-13-0.025 g	P5BBr5-250-13-0.05 g	P5BBr5-250-13-0.1 g

3. Results and discussion

3.1. Characterization of composite photocatalysts

3.1.1. XRD

The XRD pattern of the prepared photocatalyst clearly revealed the presence of the composite $PbBiO_2Br$/GO and $PbBiO_2Br$ diffraction patterns (Fig. 1). All prepared photocatalysts and composite photocatalysts contained GO and the $PbBiO_2Br$ phase (JCPDS 038-1008) [41]. Fig. 1(a, b) displays the XRD pattern of the prepared photocatalyst that clearly indicated the presence of the $PbBiO_2Br$, Bi_2O_3, and $PbBiO_2Br/Bi_2O_3$ composite phases. At the hydrothermal reaction conditions of a molar ratio of $Pb(NO_3)_2{\cdot}H_2O$:$Bi(NO_3)_3{\cdot}5H_2O$:KBr = 5:5:5, pH = 13, reaction temperature = 250 °C, and reaction time = 12 h, the XRD patterns indicated a pure crystalline phase of $PbBiO_2Br$. For other hydrothermal conditions, the XRD pattern indicated the $PbBiO_2Br/Bi_2O_3$ binary phase. At GO = 0 g, the XRD pattern was the same as that recorded for the pure $PbBiO_2Br$ phase. At GO = 0.005–0.1 g, the XRD pattern was identified as the $PbBiO_2Br$/GO binary phase.

3.1.2. TEM

The TEM pattern (Fig. 2) indicated that $PbBiO_2Br$/GO consists of layers of different sizes, consistent with the SEM (Fig. 3) observations. In addition, the EDS spectrum indicated that the composite photocatalyst contained elements of Pb, Bi, Br, O, and C. The HR-TEM images (Fig. 2c) revealed a set of lattice images with a d-spacing of 0.1457 nm corresponding to the (2 0 6) crystal plane of $PbBiO_2Br$, highly consistent with the XRD pattern (Fig. 1). These results revealed that the $PbBiO_2Br$/GO-composite phase was produced in the sample. $PbBiO_2Br$/GO thus produces high photocatalytic activity and is beneficial to the separation of the light-inducing carriers.

3.1.3. Morphological structure and composition

Fig. 3 displays the high-magnification FE-SEM images of four photocatalyst samples are displayed. According to crystal morphology observations, the $PbBiO_2Br$ and $PbBiO_2Br$/GO samples had thick polygonal, square, and irregular-shaped plates, respectively. The SEM-EDS results indicated that the main elements in these samples are Pb, Bi, Br, O, and C. The contents are detailed in Table 2.

3.1.4. XPS

The Pb 4f, Bi 4f, Br 3d, O 1s, and C 1s XPS spectra of the $PbBiO_2Br$/GO composite are displayed in Fig. 4. The transition peaks containing the Bi 4f, Pb 4f, O 1s, Br 3d, and C 1s orbitals confirmed that the catalyst comprised Bi, Pb, O, Br, and C, respectively. Fig. 4 also displays the full width at half maximum and peak energy of the Pb 4f, Bi 4f, Br 3d, O 1s, and C 1s XPS spectra, fitted by the Gaussian function. The XPS pattern, shown in Fig. 4(a), demonstrates that the two peaks of the Pb 4f spectrum were deconvolved and that the binding energies 138.1 and 142.9 eV were attributable to Pb $4f_{7/2}$ and $4f_{5/2}$, respectively, which is possibly related to the Pb of the divalent oxidation state [42]. Kovalev et al. reported that the particle size of PbS can be correlated with an observable change in the binding energy of the Pb XPS peak. The authors reported that relative integral intensity of the peak depended on the fraction of particles in the specific region [43], which indicated that a higher successive ionic layer adsorption and reaction cycle caused the formation of a portion of larger and smaller particles on titanium nanotube surfaces. The $4f_{7/2}$ peak demonstrated two binding energies (137.2 and 138.2 eV) related to the formation of two Pb^{2+} phases in the composite. In Fig. 4(b), the Bi 4f spectrum is deconvoluted into

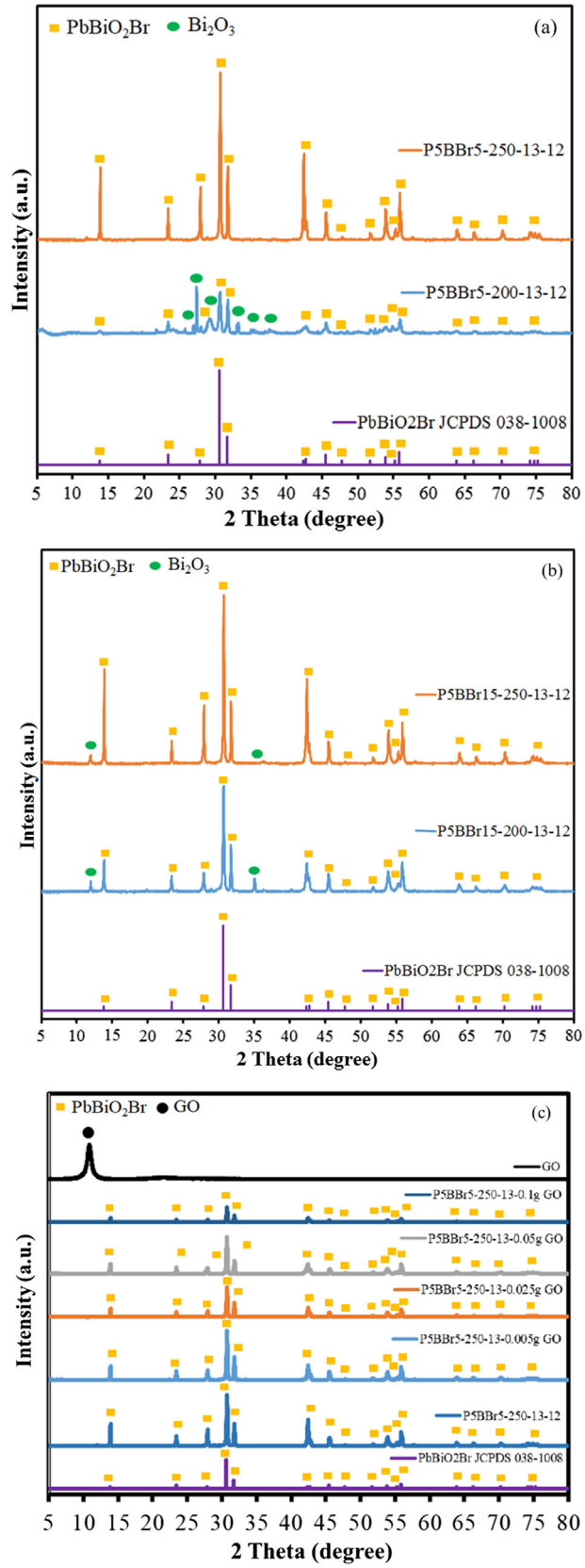

Fig. 1. (a, b) XRD patterns of as-prepared samples under different hydrothermal conditions. (molar ratio Pb/Br = 5/5, 5/15; reaction temperature = 200, 250 °C; pH = 13; reaction time = 12 h). (c) XRD patterns of as-prepared samples under different grams of GO, at reaction temperature 250 °C and reaction time 12 h. (Molar ratio Pb:Br = 5:5).

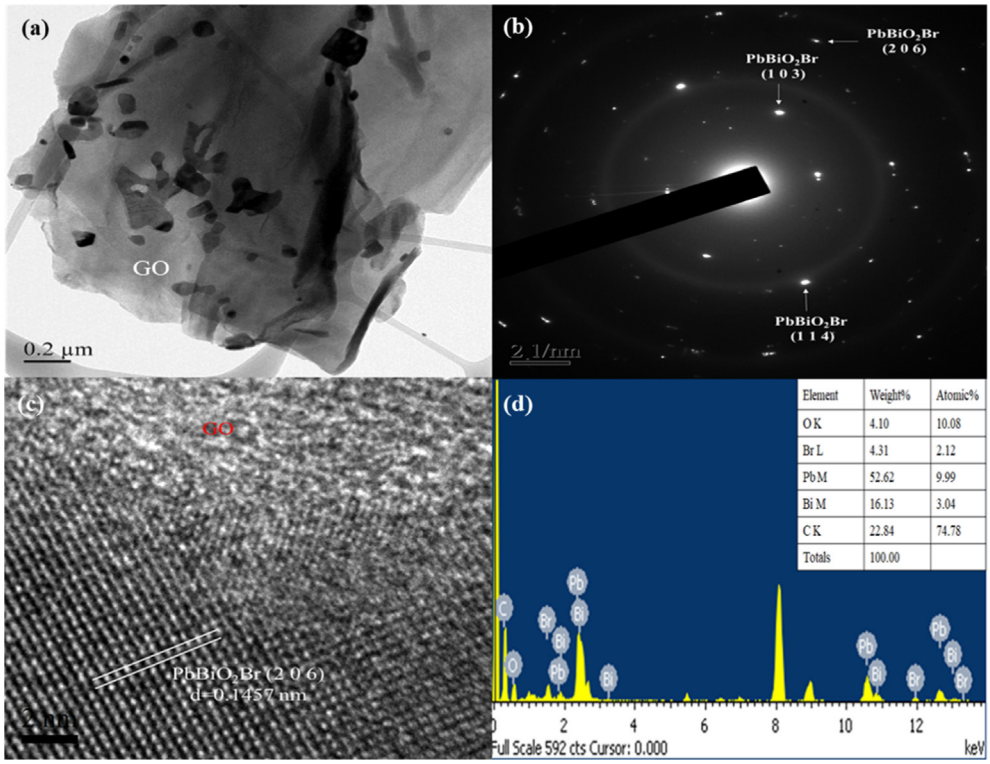

Fig. 2. P5BBr5-250-13-0.05 g GO (a) FE-TEM images, (b) SAD, (c) HR-TEM, and (d) EDS, sample by the hydrothermal autoclave method.

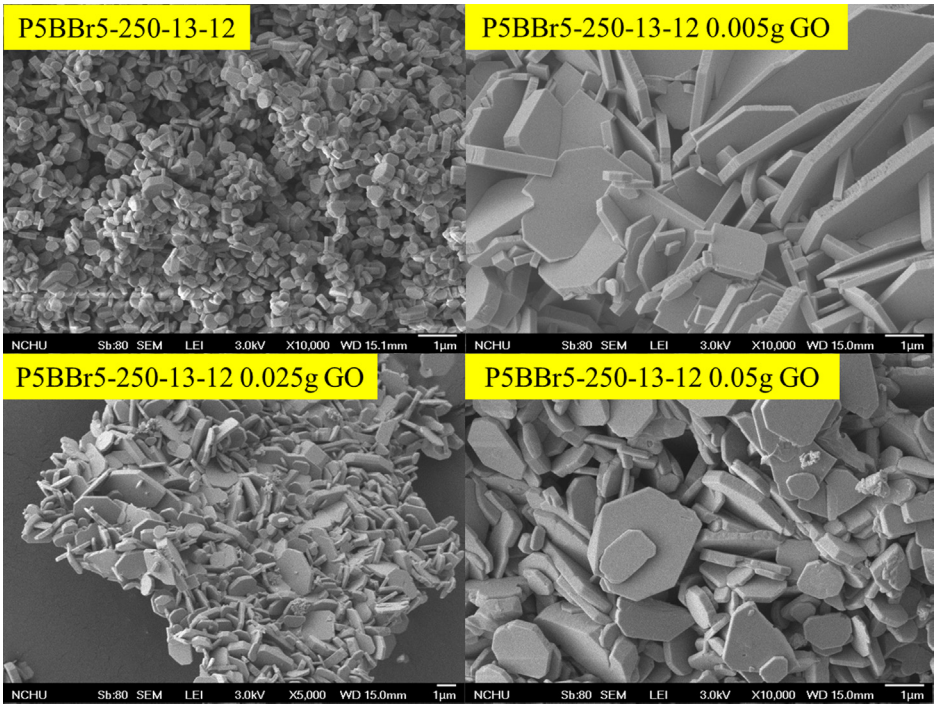

Fig. 3. SEM images of as-prepared samples by the hydrothermal autoclave method at different grams of GO. (Molar ratio Pb:Br = 5:5, temp = 250 °C, time = 12 h).

the two peaks of Bi $4f_{7/2}$ and $4f_{5/2}$. The characteristic binding energy values of 159.0 and 164.2 eV indicated a trivalent oxidation state of bismuth. Liao et al. [44] also reported similar binding energies of Bi $4f_{7/2}$. The asymmetric O 1s peak, shown in Fig. 4(c), can be split using the XPS peak-fitting program, where the peak at 531.8 eV is assigned to the external —OH group or the water molecule adsorbed on the surface and the other O 1s peak appearing at 529.8 eV corresponds to lattice oxygen atoms in $PbBiO_2Br$/GO [45]. As shown in Fig. 4(d), the binding energies of 68.8 and 70.1 are attributable to Br $3d_{5/2}$ and $3d_{3/2}$, respectively, which is attributable to the monovalent oxidation state of Br of $PbBiO_2Br$. Fig. 4(e) displays the HR C1s spectrum of the composite. Three carbon

Table 2
EDS of as-prepared samples prepared under different reaction conditions. (Pb:Br = 5:5, [Bi^{3+}] = 5 mmol, pH = 13, temp = 250 °C, time = 12 h).

Sample code	EDS of atomic ratio (%)				
	Pb	Bi	O	Br	C
P5BBr5-250-13-12	20.90	20.11	41.65	17.34	–
P5BBr5-250-13-12-0.005 g GO	10.10	10.98	33.16	10.10	35.66
P5BBr5-250-13-12-0.025 g GO	11.13	11.28	31.53	9.95	36.10
P5BBr5-250-13-12-0.05 g GO	10.93	12.57	27.98	10.38	38.13

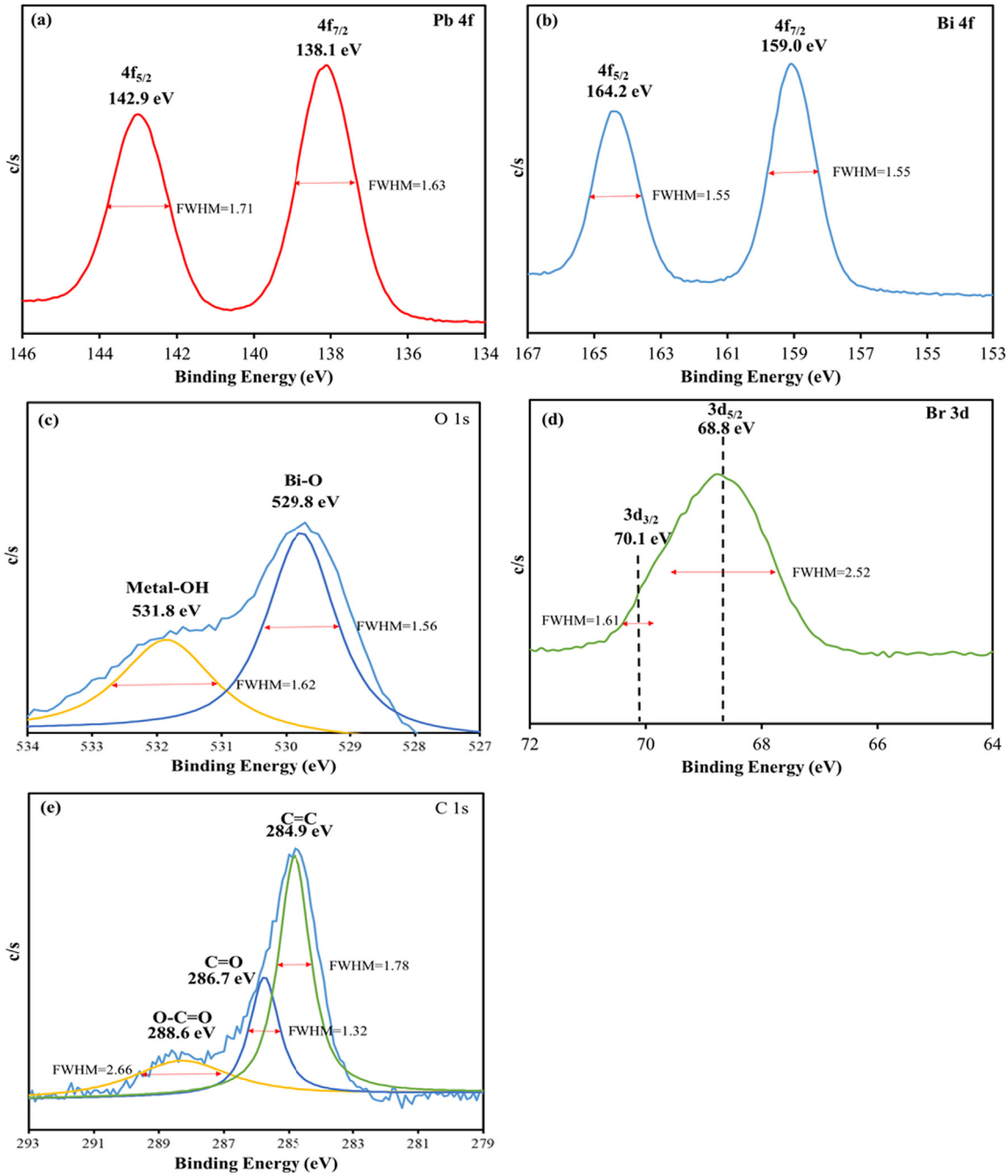

Fig. 4. XPS spectra of as-prepared samples of P5BBr5-250-13-0.05 g GO, at reaction temperature 250 °C and reaction times 12 h. (Molar ratio Pb:Br = 5:5) (a) Pb 4f; (b) Bi 4f ; (c) O 1s;(d) Br 3d; (e) C 1s.

species are mainly displayed on the C 1s spectrum at 284.9, 286.7, and 288.6 eV: the sp^2 C=C bond, the sp^2 hybridized carbon in the O-containing aromatic ring (C=O), and the sp^2 hybrid in the O—C that contains an aromatic ring (O—C=O), respectively [46,47].

3.1.5. Optical absorption properties

Pure phase $PbBiO_2Br$ absorbs only a small amount of visible light. GO is a black substance that absorbs a large amount of visible light. In a photocatalyst compound containing a small amount of

GO, the baseline of its absorption spectrum will increase, but the absorption edge of the sample is still obvious, so its band gap can be calculated. According to Fig. 5, for the DR-UV of the prepared sample, the absorption edge of the sample was 506.1–563.6 nm and, consistent with the results of a previous study, the band gap was 2.20–2.45 eV [44]. The E_g value of P5BI15-200-13-0.05 g GO ($PbBiO_2Br$/GO) was determined from the plot of $(\alpha h\nu)^{1/2}$ against energy ($h\nu$), and the calculated energy gap was 2.40 eV.

3.1.6. BET and the adsorption–desorption isotherm

The nitrogen adsorption–desorption isotherm curve of $PbBiO_2$-Br/GO is illustrated in Fig. 6. In the high relative pressure ranging between 0.9 and 1.0, the isotherm of $PbBiO_2Br$/GO is close to type III without hysteresis loops [48]. Such self-organized porous structures can be highly useful in photocatalysis because they provide an efficient transport route for reactants and product molecules [49]. The S_{BET} of the P5BI15-200-13-0.05 gGO ($PbBiO_2Br$/GO) sample was measured to be approximately 0.75 $m^2\ g^{-1}$. The pore volume and diameter of the composite sample were determined to be 0.0046 $cm^3\ g^{-1}$ and 586.4 nm, respectively. The S_{BET} of the $PbBiO_2$-Br sample was approximately 1.59 $m^2\ g^{-1}$, and the pore volume and diameter of the composite sample were determined to be 0.02 $cm^3\ g^{-1}$ and 534.1 nm, respectively. The corresponding pore size distribution (PSD) of the PbBiO2Br/GO photocatalyst sample is shown in Fig. 6**(b)**. The PSD curve of the PbBiO2Br/GO sample is bimodal, indicating medium mesopores (10–50 nm) and large macropores (50–290 nm). Because the nanosheets do not contain pores (Fig. 3), smaller mesopores may reflect the pores within the nanosheets. Medium mesopores can be attributed to the pores formed between the stacked nanoplates, while large macropores can be attributed to the pores formed between the nanoplatelets. Such self-organized porous structures can be very useful in photocatalysis because they provide efficient transport pathways for reactant and product molecules. The nanosheet structure can also provide an effective transmission path for reactants and provide more active sites for photocatalytic reactions. This structure also facilitates efficient light energy collection and separation of electron-hole pairs, thereby enhancing photocatalytic activity. This result is consistent with the FE-SEM result, which indicates that a 3D layered structure is formed by the self-assembled nanosheet or nanoplate.

3.2. Photocatalytic activity

The degradation efficiency and rate constant as functions of reaction time are illustrated in Fig. 7 and Table 3, respectively. In

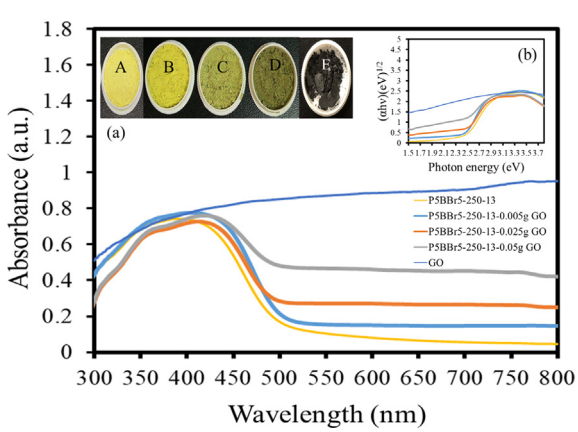

Fig. 5. UV–vis absorption spectra of the as-prepared photocatalysts of different grams GO. (Molar ratio Pb:Br = 5:5, reaction temp = 250 °C, reaction time 12 h).

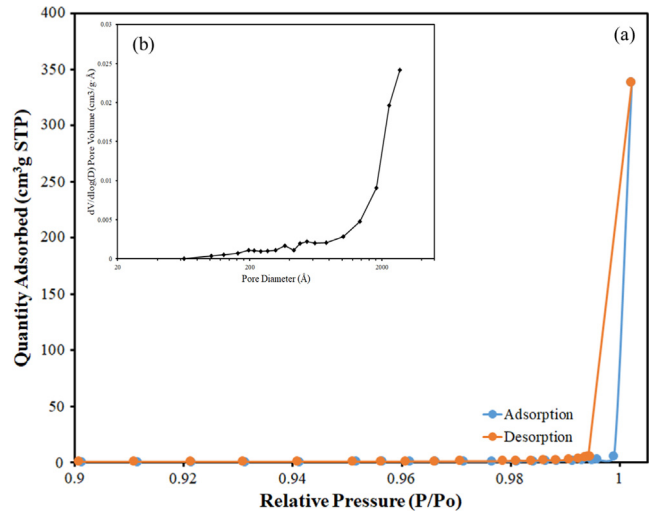

Fig. 6. (a)Nitrogen adsorption-desorption isotherms and (b) the corresponding pore size distribution curve (inset) for P5BBr5-250-13-0.05 g GO.

the presence of a composite photocatalyst, the removal efficiency improved significantly. After 48 h of irradiation, P5BI15-200-13-0.05gGO (PbBiO2Br/GO) had excellent photocatalytic performance and a CV removal rate was 98.6%. To further understand the reaction kinetics of CV degradation, the apparent pseudo-first-order model [50], $\ln(C_o/C) = kt$, was applied in the experiments. The k value of P5BI15-200-13-0.05gGO ($PbBiO_2Br$/GO) was obtained by a first-order linear fitting of the data. The maximum degradation rate was $1.278 \times 10^{-1}\ h^{-1}$, which was higher than that of other composite materials. In addition, the catalytic performance indicated that the optimal reaction rate constant of CV was 0.1278 h^{-1} when 0.05 wt%-GO/$PbBiO_2Br$ composite was used as photocatalyst, 1.82 times that of $PbBiO_2Br$ when $PbBiO_2Br$ was used as a photocatalyst.

The degradation efficiency and rate constant of 2-hydroxybenzoic acid (2-HBA) as functions of reaction time are illustrated in Fig. 8. The catalytic performance indicated that the optimal reaction rate constant of 2-HBA was 0.0093 h^{-1} when 0.05 wt%-GO/$PbBiO_2Br$ composite was used as a photocatalyst, 1.24 times the reaction rate constant of $PbBiO_2Br$ when $PbBiO_2Br$ was used as a photocatalyst.

Under optimal synthesis conditions, the photocatalytic activity of the $PbBiO_2Br$/GO composites was much higher than that of $PbBiO_2Br$. Under 432-nm visible light irradiation, 25 °C temperature, and 1-atm pressure, the optimized $PbBiO_2Br$/GO increased the rate (at 2.386 μmol $g^{-1}\ h^{-1}$) of photocatalytic conversion from CO_2 to CH_4. This increase was higher than that induced by the original $PbBiO_2Br$ material (at 1.193 μmol $g^{-1}\ h^{-1}$). Therefore, $PbBiO_2$-Br/GO has obvious advantages in the production of CH_4 and has great potential for the production of CO_2 photoreduction catalysts.

The enhanced photocatalytic activity of the composite is attributable to synergistic effects from layered structures, low energy band structures, a high BET surface area, and the formation of heterojunctions. To investigate the BET surface area in the heterostructure, the BET surface area of the $PbBiO_2Br$/GO sample was measured. The lower BET surface area of the $PbBiO_2Br$/GO composites indicates that they have a lower photocatalytic activity. Generally, after irradiation in a photocatalytic process, the photocatalyst is excited to directly generate electron–hole pairs. In addition, the photocatalytic efficiency is mainly determined by the recombination rate or lifetime of photogenerated electron–hole pairs. The faster the recombination, the slower the chemical reaction.

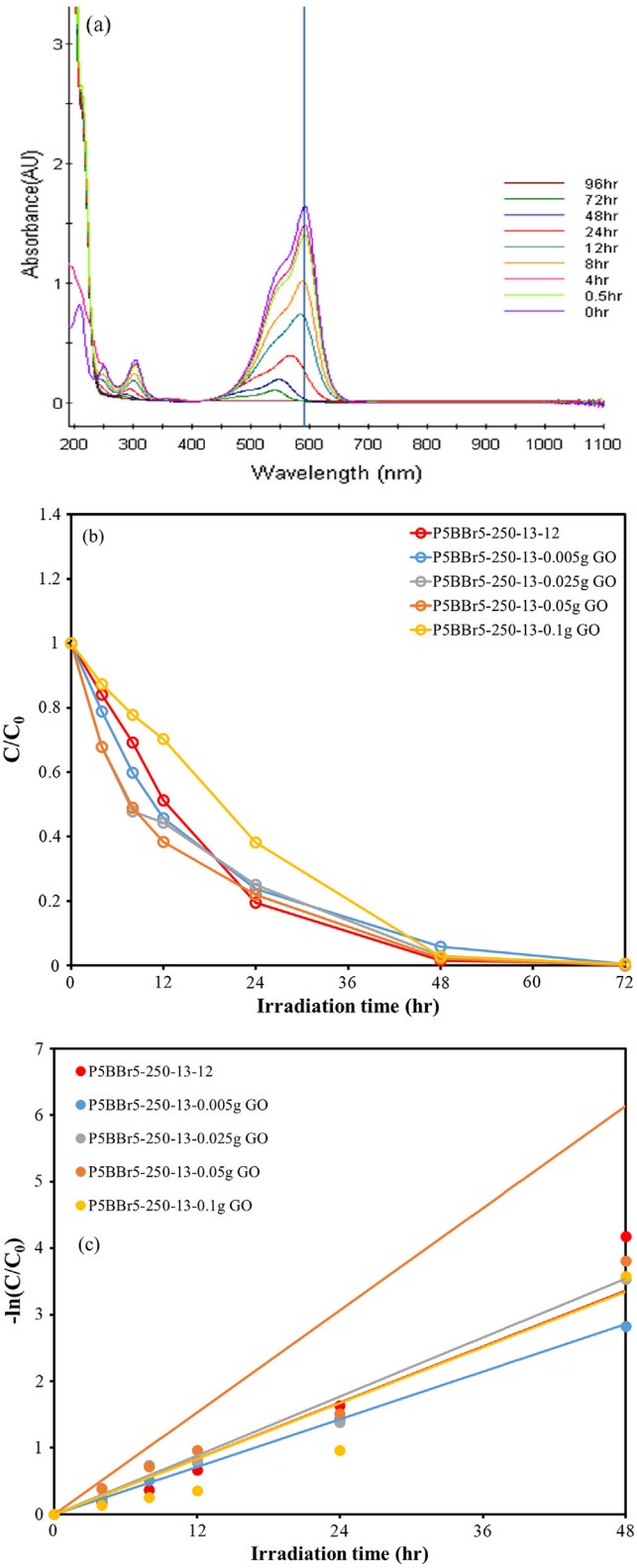

Fig. 7. (a) Photocatalytic degradation of CV as a function of irradiation time over photocatalysts, (b) Photocatalytic degradation of CV as a function of irradiation time over different grams of GO. (Molar ratio Pb:Br = 5:5, pH = 13, reaction temperature = 250 °C, reaction time 12 h).

Therefore, the PL spectrum was used to investigate the recombination rate of photogenerated electron–hole pairs. To study the separation ability of photogenerated carriers in a heterostructure,

Table 3
Pseudo-first-order rate constant for CV photocatalytic oxidation under different photocatalysts.

Photocatalyst	k (h^{-1})	R^2
P5BBr5-250-13	0.0701	0.9984
P5BBr5-250-13-0.005 g	0.0595	0.9987
P5BBr5-250-13-0.025 g	0.1040	0.7831
P5BBr5-250-13-0.05 g	0.1278	0.8660
P5BBr5-250-13-0.1 g	0.0698	0.9625

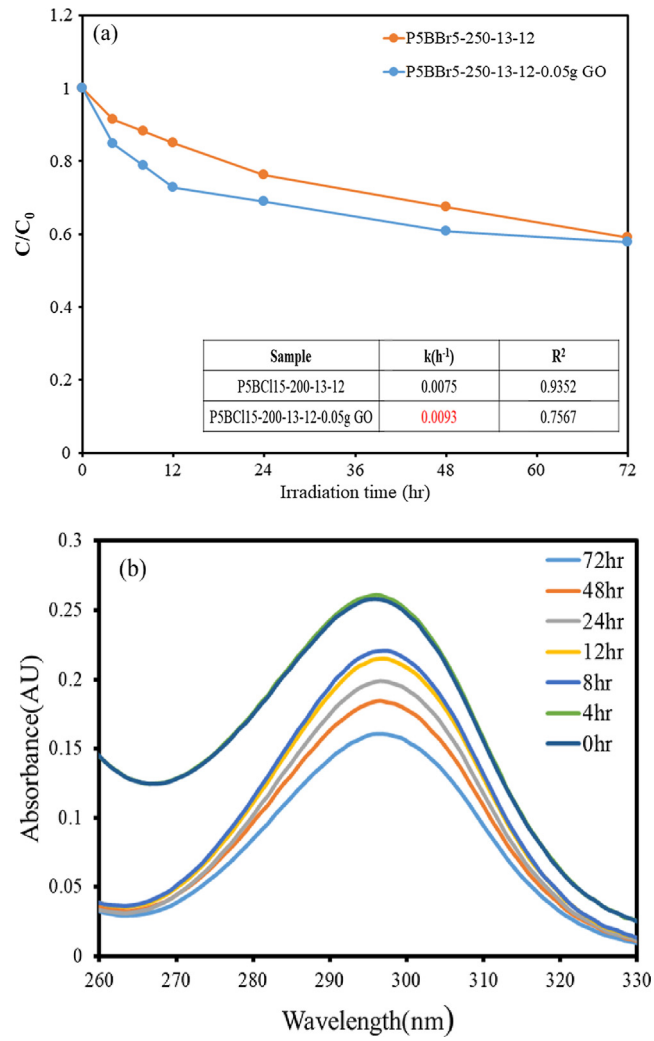

Fig. 8. (a)Photocatalytic degradation of 2-hydroxybenzoic acid (2-HBA) as a function of irradiation time over photocatalysts, (b) Photocatalytic absorption spectrum (Molar ratio Pb:Br = 5:5, pH = 13, reaction temperature = 250 °C, reaction time 12 h).

$PbBiO_2Br$/GO, $PbBiO_2Br$, and GO samples were measured, and their PL spectra are displayed in Fig. 9. The spectrum of the prepared sample had a strong emission peak at approximately 490 nm, which is derivable from direct electron–hole recombination with transition. However, the characteristic emission peak near the lowest intensity of 490 nm for $PbBiO_2Br$/GO indicates that the effective separation of charge can increase the lifetime of charge carriers and increase the efficiency of interface charge transfer to the adsorbed substrate, thereby improving photocatalytic activity. The photocatalytic activity of the $PbBiO_2Br$/GO heterojunctions reached the maximum rate constants of 0.1278 h^{-1}, 0.0093 h^{-1}, and 1.913 μmol g^{-1} h^{-1}, which were 1.82, 1.24, and 2.00 times

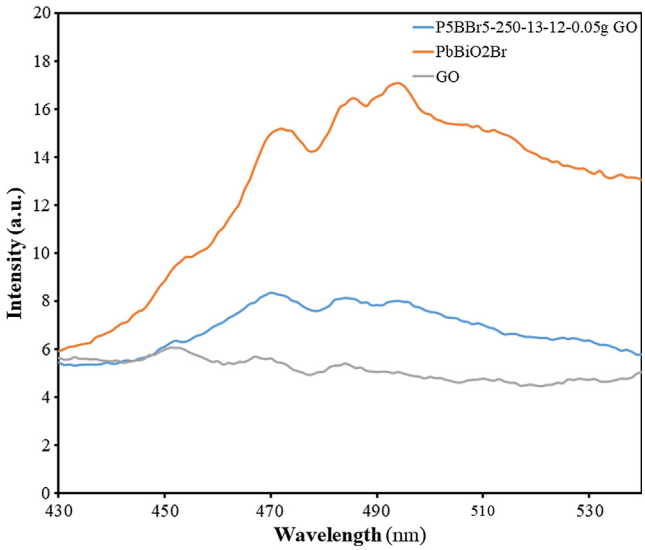

Fig. 9. Photoluminescence (PL) spectra of the as-prepared photocatalysts.

higher than those of $PbBiO_2Br$ in CV degradation, 2-HBA degradation, and CO_2 photocatalytic reduction, respectively. Thus, the $PbBiO_2Br$/GO heterojunctions may also play a role in enhancing photocatalytic activity. The PL results confirm the importance of the composites in hindering electron–hole recombination, thus explaining the reason for the increased photocatalytic performance of the $PbBiO_2Br$/GO composites.

We recycled $PbBiO_2Br$/GO to prove that it is an effective and durable photocatalyst. We performed centrifugation to ensure that we could collect the photocatalyst after each cycle. As illustrated in Fig. 10(a), no significant performance loss occurred in CV removal efficiency in the fourth cycle. Even in the fifth cycle, photocatalyst performance decreased only by 4.47%.

In et al. [51] reported that a novel G-TNT photocatalyst was composed of electrodeposited graphene quantum dots (GQD) on sensitized TiO_2 nanotube arrays (TNT). Under solar light irradiation, it found optimal G-TNT samples promoting a CO_2 to CH_4 photocatalytic conversion rate of 1.98 ppm cm^{-2} h^{-1}. In and the coworkers [52] synthesized TNT films sensitized with rGO-TiO_2 nanoparticles (rGO-TNTNP). The conversion rate of rGO-TNTNP photocatalytically generated CH_4 (5.67 ppm cm^{-2} h^{-1}) was about 4.4 times higher than that of pure TNT sample (1.28 ppm cm^{-2} h^{-1}). These studies found enhanced photoelectrochemical and photocatalytic performance, which led to our hypothesis that enhanced graphene deposition technology could provide higher material homogeneity and should have higher activity in the photocatalytic conversion of CO_2 to CH_4.

According to Fig. 10(b), CH_4 yield in the second cycle demonstrated a significant performance loss. In the third cycle, the production efficiency of CH_4 decreased to 1.037 μmol g^{-1} h^{-1}. As for the production of CH_4 in the fourth and fifth cycles, the efficiencies were 0.965 and 0.927 μmol g^{-1} h^{-1}, respectively, with no significant performance loss. As illustrated in Fig. 10(c), the recycled $PbBiO_2Br$/GO was also measured by XRD; no significant difference was found between the repeatedly used and as-synthesized composite materials. Therefore, the photocatalytic stability of $PbBiO_2Br$/GO is favorable.

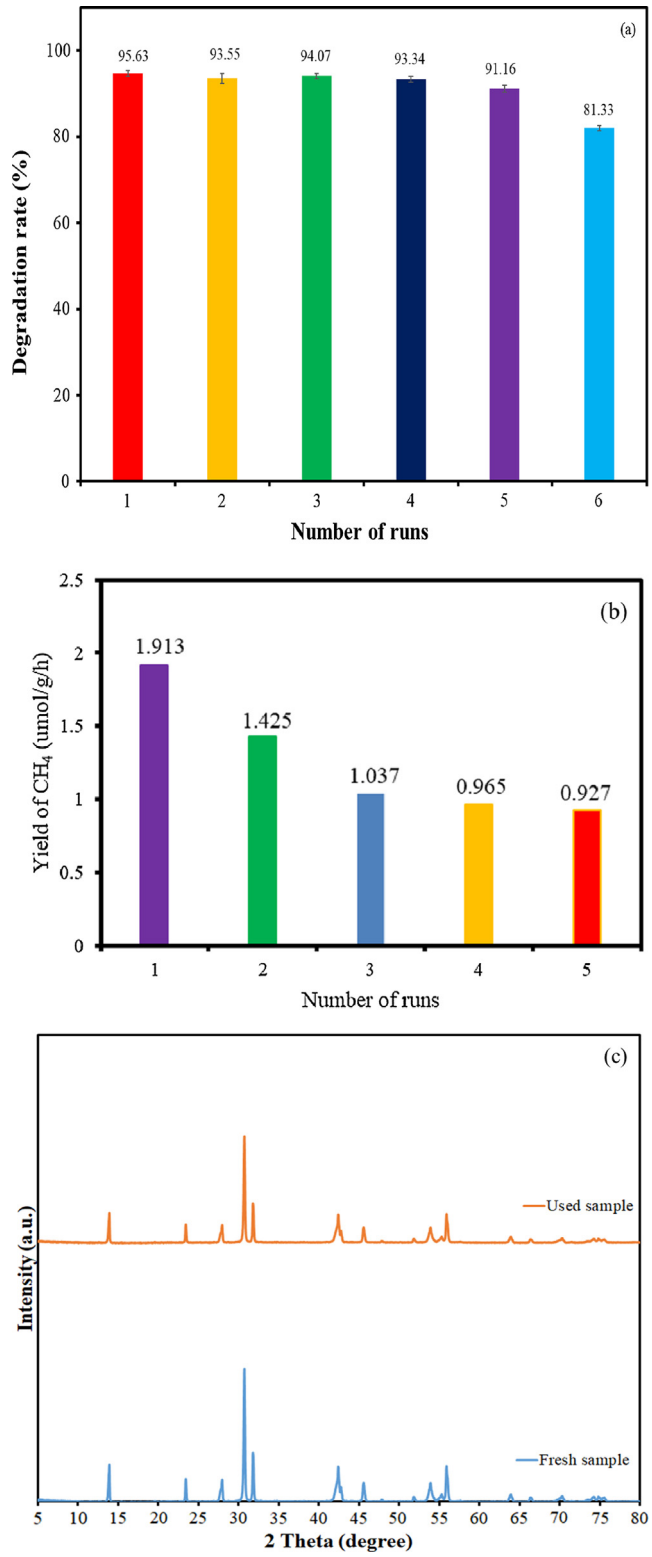

Fig. 10. Cycling runs of (a) CV and (b) CO_2, and (c) XRD patterns acquired before and after in the photocatalytic degradation of CV in the presence of P5BBr5-250-13-0.05 g GO.

3.3. Photocatalytic degradation mechanisms

During the photocatalytic degradation of UV–Vis/semiconductor systems, various major active substances, such as ·OH, h^+, O_2^{-}·, ·H, and $^1O_2$, may be produced [53]. To evaluate the role of the active substance in the photocatalytic reaction, different quenchers were used to remove the relevant active substance. Combining GO with other materials results in electrons that flow from one material to another (i.e., from a high to low Fermi level); this results in Fermi level alignment at the GO–material interface [54]. As Wang et al. demonstrated [55], O_2^{-}· and ·OH radicals are the main active sub-

stances for rhodamine B degradation with $BiVO_4$/rGO. The ·OH radical may be formed only in the $e^- \rightarrow O_2^{-\cdot} \rightarrow H_2O_2 \rightarrow$ ·OH pathway. However, the ·OH radical is formed through multistep $O_2^{-\cdot}$ reduction. Studies have reported that $O_2^{-\cdot}$ photocatalytic processes are the main active species, rather than the ·OH, e^-, or h^+ active species. Bai et al. [56] demonstrated that the capture measurement of active species that contain $O_2^{-\cdot}$ and ·OH radicals is critical for using $ZnWO_4$/graphene hybrids to catalyze methylene blue degradation. Li et al. [57] used BiO_mX_n/BiO_pY_q (X, Y = Cl, Br, I) under visible light irradiation and demonstrated that oxidation dominates the CV degradation process and that the main active species is $O_2^{-\cdot}$ but the secondary active species is ·OH and h^+. The results of these studies indicate that the probability of ·OH formation is lower compared with that of $O_2^{-\cdot}$ formation. However, ·OH is powerful and nonselective and it induces the partial or complete mineralization of several organic chemicals.

In Fig. 11(a), four strong characteristic peaks of the DMPO-·OH adduct (quartet pattern, 1:2:2:1) of the $PbBiO_2Br$/GO dispersion on irradiation under visible light are absent. Fig. 11(b) illustrates six characteristic peaks of a DMPO-$O_2^{-\cdot}$ adduct [58] that illuminates the $PbBiO_2Br$/GO dispersion under visible light. Fig. 11(a) and 11(b) indicates that no EPR signal is observed when the reaction is carried out in the dark and that the intensity corresponds to the signal of the characteristic peak of the DMPO-$O_2^{-\cdot}$ adduct under visible light irradiation. Moreover, during the process, $O_2^{-\cdot}$ is formed as an active material under visible light irradiation in the presence of $PbBiO_2Br$/GO and oxygen.

In this study, the effects of active substances in a photocatalytic reaction were re-evaluated by introducing several quenchers and thus the relevant active species were eliminated. As illustrated in Fig. 11(c), the introduction of AO did not affect the photocatalytic degradation of CV. However, the quenching of BQ, IPA, and SA clearly reduced the degradation efficiency. In the photocatalytic degradation of CV, $O_2^{-\cdot}$ and $^1O_2$ were the two main active substances. Therefore, the observed scavenger and EPR-induced quenching effects indicated that $O_2^{-\cdot}$ and $^1O_2$ play major roles in the aforementioned degradation, whereas ·OH and h^+ play minor roles.

Fig. 12 illustrates the photocatalytic degradation and photocatalytic reduction based on the results of the foregoing experiments. Fig. 12(a) suggests that after the electron reaches the $PbBiO_2Br$ conduction band, it immediately generates active oxygen species, causing the CV dye to decompose. The photosensitization and photocatalytic processes are also simultaneous. However, under the conditions that are associated with photosensitization and photocatalytic reactions, photogenerated and photosensitized electrons react with photocatalyst-surface-adsorbed oxygen to produce $O_2^{-\cdot}$ radicals. In addition, $O_2^{-\cdot}$ radicals react with H^+ ions, and the h^+ hole reacts with the OH^- ion (or H_2O) to generate a hydroxyl radical. These sequences result in the production of hydroxyl radicals [59]. Under irradiation with visible light, the illumination system causes the continuous occurrence of this cycle [60]. Unexpected $^1O_2$ formation mechanism was predicted during the photoexcitation of the $PbBiO_2Br$/GO photocatalyst. It is also possible to produce $^1O_2$ by transferring electrons between superoxide $O_2^{-\cdot}$ and cationic species (H^+ or h^+) under the appropriate oxidizing power [61]. A study [62] reported the mechanism of $^1O_2$ formation during the photoexcitation of ZnO, in which the photogenerated h^+ by the photocatalyst acts as a cationic species that oxidizes $O_2^{-\cdot}$.

Eqs. (1)–(3) represent the decomposition process of CV or HBA, which is caused by the photogenerated oxidant species; it is a recycling step.

$$\text{CV (HBA)} + O_2^{-\cdot} \rightarrow \text{photodegraded products} \quad (1)$$

$$\text{CV (HBA)} + {}^1O_2 \rightarrow \text{photodegraded products} \quad (2)$$

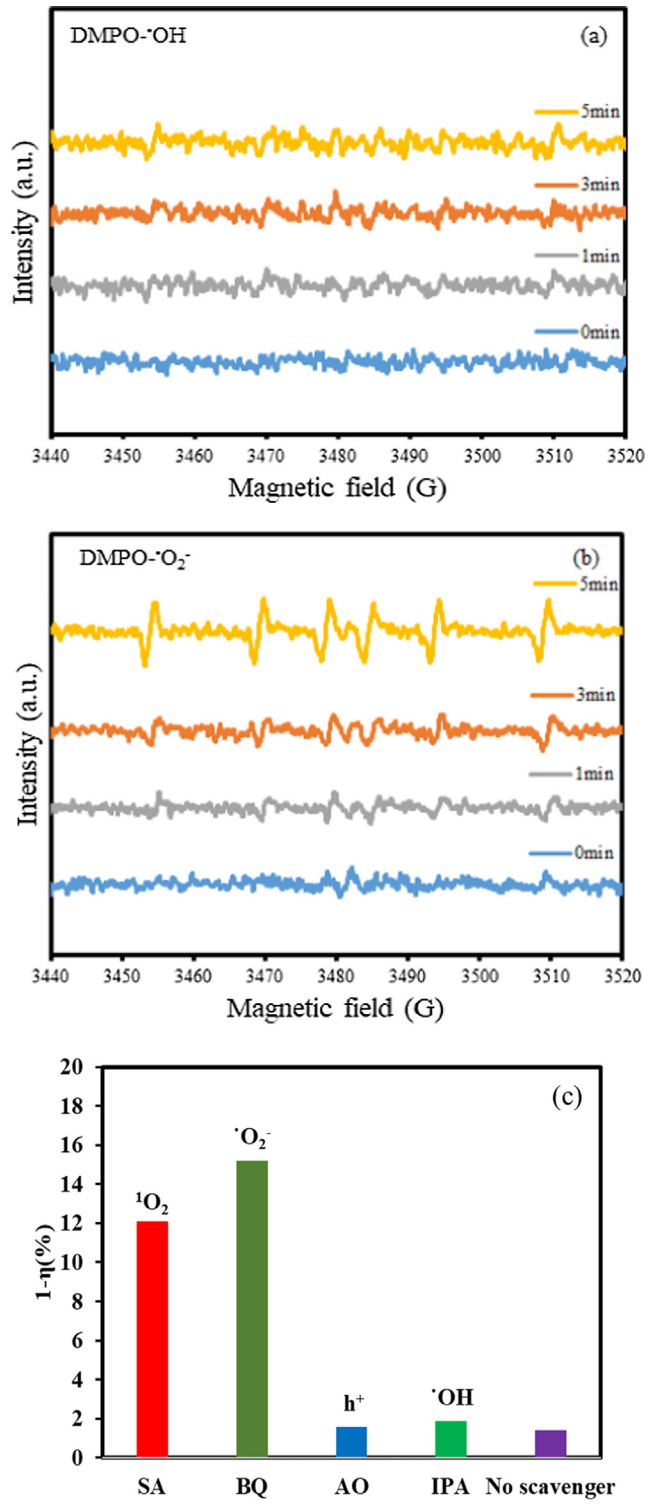

Fig. 11. (a) EPR spectra in the methanol dispersion for DMPO-·OH; (b) EPR spectra in aqueous solution dispersion for DMPO-$O_2^{-\cdot}$; (c) trapping experiment of active species during the photocatalytic reaction using $PbBiO_2Br$/GO (Molar ratio Pb: Br = 5:5, reaction temp = 250 °C, reaction time 12 h, 0.05 g GO).

$$\text{CV (HBA)} + OH^{\cdot} \rightarrow \text{photodegraded products} \quad (3)$$

This study has identified hydroxylated compounds produced by the photocatalytic degradation of CV by visible light–driven semiconductor systems [45,57,59,60]. In previous studies, under the process of the photocatalytic degradation of CV dye by ultraviolet

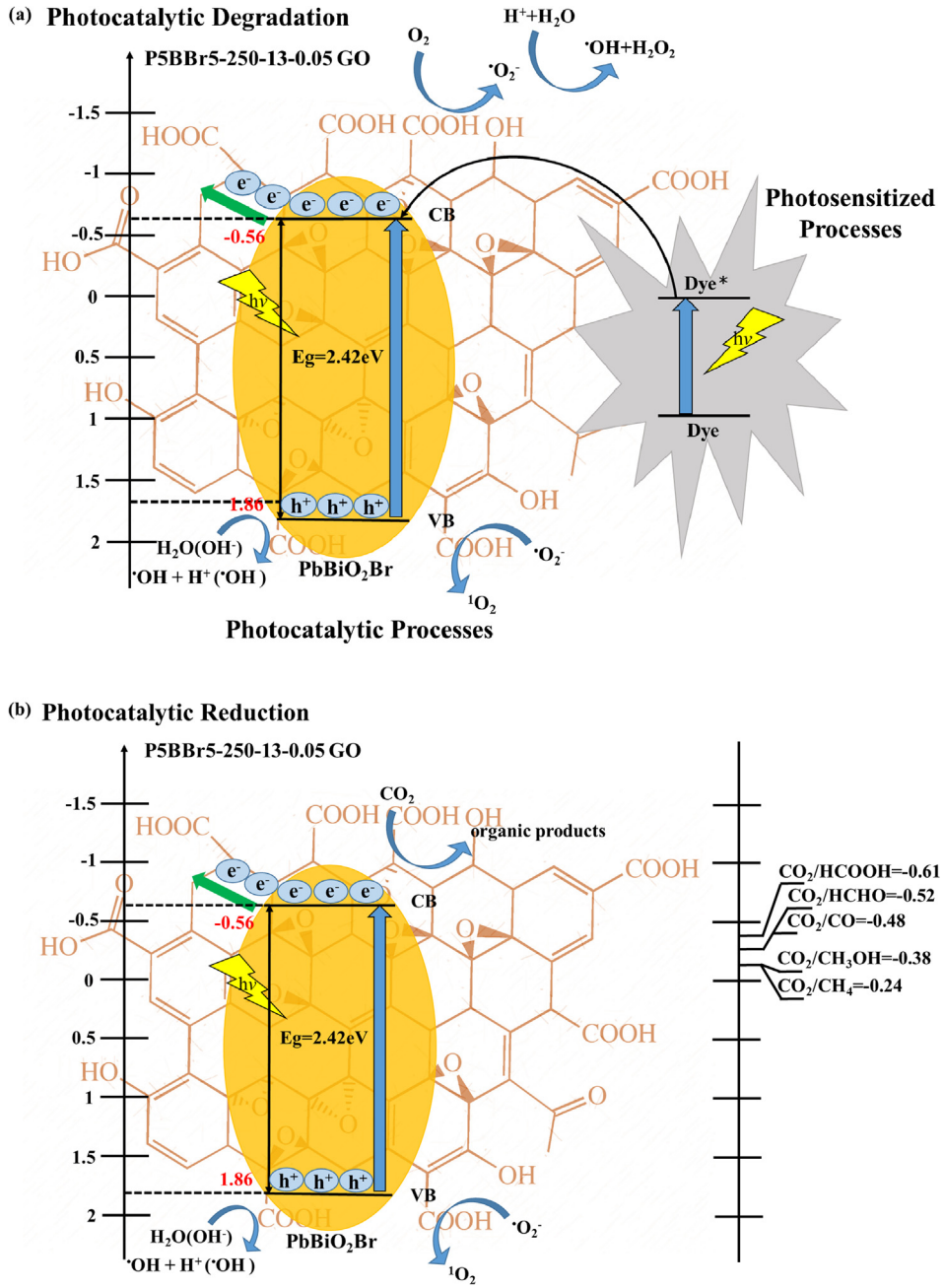

Fig. 12. The band structure diagram and the possible charge separation processes of $PbBiO_2Br$/GO for (a) photocatalytic degradation and (b) photocatalytic reduction.

light irradiation, nitrogen-centered free radical formation has been observed before *N*-dealkylation, and carbon-centered free radicals have been established before the dye chromophore structure are destroyed [45,59,60]. In two different systems (under UV and visible light illumination), all identified intermediates were identical, thus yielding the same results. The photocatalysis and photoactivation processes are simultaneous but $O_2^{-\cdot}$ is generated by O_2 on the surface of the catalyst with photogenerated and photosensitized electrons, whereas ·OH results from O_2^{-}, with H^+ and h^+ in the OH^- (or H_2O) reactions. Notably, ·OH may be produced only by the $e^- \rightarrow O_2^{-\cdot} \rightarrow H_2O_2 \rightarrow$ ·OH process, wherein ·OH is produced by multistep reduction of $O_2^{-\cdot}$; the major oxidant is ·OH, rather than $O_2^{-\cdot}$. The proposed reaction pathway for the supported-$PbBiO_2Br$/GO photocatalytic process can be used as a guide for CV or HBA decomposition.

Falaras et al. [63] reported the intermediates for the photocatalytic degradation of 2-HBA by titanium dioxide nanotubes (TNTs). Variations on the degradation efficiency were observed between them at alkaline and acidic pH values, whereas the TNTs showed slightly increased photocatalytic performance probably due to easier removal of the formed intermediates from the TNT highly porous surface.

We observed that optimally, $PbBiO_2Br$/GO promotes (at 1.913 μmol g^{-1} h^{-1}) the rate of CO_2 to CH_4 photocatalytic conversion at 25 °C under 1 atm, much higher than that of original $PbBiO_2Br$ material (at 0.957 μmol g^{-1} h^{-1}), which indicate that $PbBiO_2Br$/GO has a decisive advantage in CH_4 production and great potential in applications involving CO_2 conversion catalysis. Removal and conversion efficiency is significantly enhanced in the presence of $PbBiO_2Br$/GO. A reaction mechanism of the CO_2

photocatalytic reduction for the $PbBiO_2Br$/GO photocatalyst is proposed in Fig. 12(b). Studies on the photochemical reduction of CO_2 (which was adsorbed in water) have indicated that H_2CO_3 and dissolved CO_2 are likely to be active substances [64,65]. The equilibrium equations for carbon dioxide in an alkaline solution are

$$CO_2 + H_2O \rightarrow H_2CO_3 \quad (4)$$

$$H_2CO_3 + OH^- \rightarrow H_2CO_3^- + H_2O \quad (5)$$

$$H_2CO_3^- + OH^- \rightarrow CO_3^{2-} + H_2O \quad (6)$$

Because HCO_3^- and CO_3^{2-} have negligible improvements in catalytic performance, the main carbonaceous substances involved in alkali-enhanced reduction are considered H_2CO_3 and dissolved CO_2. That is, H_2CO_3 is more likely to be the main form of CO_2 reduced during photocatalysis. Zhong et al. [66] reported the variation of inorganic carbon species in different electrolytes. The authors observed that after bubbling with CO_2, the ratio of H_2CO_3 to total inorganic carbon species (H_2CO_3, CO_2, HCO_3^-, and CO_3^{2-}) in a low initial concentration of 0.1 M $KHCO_3$ was lower than that in 0.1 M KOH. However, if the KOH concentration increases, this value decreased significantly. Thus, similar to our NaOH decorative samples, a small amount of OH^- can dynamically maintain a stable amount of H_2CO_3 in a thin layer of solution on the surface of photocatalyst. The photocatalytic process, with OH^- as hole scavengers, subsequently consumes the stabilized H_2CO_3 before it changes to HCO_3^- or CO_3^{2-}. The formation and consumption cycle of H_2CO_3 can thus be conceived. In other words, the cycle of H_2CO_3 in photocatalytic conversion and regeneration can be sustained, and it must be maintained at a relatively low concentration of OH^-. If the concentration of OH^- is too high, the H_2CO_3 equilibrium may be destroyed, resulting in the conversion of H_2CO_3 to HCO_3^- and CO_3^{2-}. In addition, a larger concentration of alkali on the surface of the photocatalyst also inhibits the transfer of photoexcited charges from the photocatalyst surface to the reactive species [66]. The initial enhancement of CH_4 formation by $NaHCO_3$-$PbBiO_2Br$/GO, as illustrated in Fig. 10(b), can be inferred from $NaHCO_3$ being deliquefied on a thin layer of the photocatalyst surface and HCO_3^- coexisting with H_2CO_3 (according to Eqs. (4)–(6)). When the sample is irradiated, H_2CO_3 participates in the reaction. However, $NaHCO_3$ exhibited an inferior ability to adsorb water, resulting in lower concentrations on the surface of the photocatalyst. Notably, systems with $NaHCO_3$ lack OH^- as a driving force for enhancing CO_2 adsorption and hole receptors. Consequently, the $NaHCO_3$–photocatalysts exhibited no significant enhancement relative to bare $PbBiO_2Br$/GO.

Based on the aforementioned results, the enhanced activity of photocatalytic reduction and degradation is attributable to the effective separation of photogenerated carriers. Such separation is driven by the photoinduced potential difference generated at these heterojunction interfaces, transfer of photogenerated electrons through the GO skeleton, and favorable well-aligned straddling band structure of the $PbBiO_2Br$/GO.

4. Conclusion

This study is the first to synthesize $PbBiO_2Br$/GO heterojunctions using template-free hydrothermal methods. In particular, the catalytic performance indicates that when using 0.05 wt%-GO/$PbBiO_2Br$ composite as the photocatalyst, the best reaction rate constants for CV and 2-HBA were 0.1278 and 0.0093 h^{-1}, which were 1.82 and 1.24 times higher than the reaction rate constant of $PbBiO_2Br$ when $PbBiO_2Br$ was used as a photocatalyst, respectively. We observed that optimally, $PbBiO_2Br$/GO promotes a CO_2 to CH_4 photocatalytic conversion rate (at 1.913 μmol g^{-1} h^{-1}) at 25 °C under 1 atm, much higher than that of the original $PbBiO_2Br$ material (at 0.957 μmol g^{-1} h^{-1}), which indicates the $PbBiO_2Br$/GO has an increased advantage in CH_4 production and suggests its great potential for applications involving CO_2 conversion catalysis. The removal and conversion efficiency is significantly enhanced in the presence of $PbBiO_2Br$/GO. Such enhanced photocatalytic activity is attributable to the effective separation of photogenerated carriers. Such separation is driven by the photoinduced potential difference generated at these heterojunction interfaces, transfer of photogenerated electrons through the GO skeleton, and favorable well-aligned straddling band structure of the $PbBiO_2Br$/GO. The quenching effects of scavengers indicate that reactive $O_2^{\cdot-}$ and $^1O_2$ play the major roles in the photocatalytic degradation of CV. The possible photodegradation mechanisms were proposed and discussed in this study. In general, this study provides the synthesis of $PbBiO_2Br$/GO and the photocatalysis of CV, 2-HBA, and CO_2 and evidence for its future applications in solar fuels and environmental pollution and control.

CRediT authorship contribution statement

Fu-Yu Liu: Data curation, Investigation, Writing - original draft, Methodology. **Yong-Ming Dai:** Methodology, Validation, Investigation, Software. **Fu-Hsuan Chen:** Writing - review & editing. **Chiing-Chang Chen:** Supervision, Conceptualization, Visualization, Writing - review & editing, Validation.

Declaration of Competing Interest

The authors declare that they have no known competing financial interests or personal relationships that could have appeared to influence the work reported in this paper.

Acknowledgments

This research was supported by the Ministry of Science and Technology of the Republic of China (MOST-108-2113-M-142 - 001).

References

[1] X. Li, J. Yu, M. Jaroniec, X. Chen, Chem. Rev. 119 (2019) 3962–4179.
[2] C. He, J. Cheng, X. Zhang, M. Douthwaite, S. Pattisson, Z. Hao, Chem. Rev. 119 (2019) 4471–4568.
[3] M.R. Hoffmann, S.T. Martin, W. Choi, D.W. Bahnemann, Chem. Rev. 95 (1995) 69–96.
[4] J. Kou, C. Lu, J. Wang, Y. Chen, Z. Xu, R.S. Varma, Chem. Rev. 117 (2017) 1445–1514.
[5] A. Kubacka, M. Fernández-García, G. Colón, Chem. Rev. 112 (2012) 1555–1614.
[6] Ullmann's Encyclopedia of Industrial Chemistry, Part A27. Triarylmethane and Diarylmethane Dyes, sixth ed., Wiley-VCH, New York, 2001.
[7] B.P. Cho, T. Yang, L.R. Blankenship, J.D. Moody, M. Churchwell, F.A. Bebland, S.J. Culp, Chem. Res. Toxicol. 16 (2003) 285–294.
[8] LF. De Tauxe-Wuersch, D. Alencastro, J. Tarradellas Grandjean, Water Res. 39 (2005) 1761–1772.
[9] M. Berk, O. Dean, H. Drexhage, J.J. McNeil, S. Moylan, A. O'Neil, M. Maes, BMC Med. 11 (2013) 74.
[10] A.C. Vlot, D.M.A. Dempsey, D.F. Klessig, Annu. Rev. Phytopathol. 47 (2009) 177–206.
[11] A.J. Langstieh, P. Verma, A.K. Thakur, S.S. Chatterjee, V. Kumar, Pharmacologia 5 (2014) 326–338.
[12] R. He, D. Xu, B. Cheng, J. Yu, W. Ho, Nano. Horiz. 3 (2018) 464–504.
[13] S.T. Huang, Y.R. Jiang, S.Y. Chou, Y.M. Dai, C.C. Chen, J. Mol. Catal. A: Chem. 391 (2014) 105–120.
[14] M. Long, P. Hu, H. Wu, Y. Chen, B. Tan, W. Cai, J. Mater. Chem. A 3 (2015) 5592–5598.
[15] C.C. Chen, J.Y. Fu, J.L. Chang, S.T. Huang, T.W. Yeh, J.T. Hung, P.H. Huang, F.Y. Liu, L.W. Chen, J. Colloid Interface Sci. 532 (2018) 375–386.
[16] J.Y. Fu, L.W. Chen, Y.M. Dai, F.Y. Liu, S.T. Huang, C.C. Chen, Mol. Catal. 455 (2018) 214–223.
[17] C.W. Siao, W.W. Lee, W.H. Chung, J.T. Hung, P.H. Huang, W.Y. Lin, C.C. Chen, J. Colloid Interface Sci. 544 (2019) 25–36.

[18] C.W. Siao, H.L. Chen, L.W. Chen, J.L. Chang, T.W. Yeh, C.C. Chen, J. Colloid Interface Sci. 526 (2018) 322–336.
[19] Z. Chen, H. Jiang, W. Jin, C. Shi, Appl. Catal. B: Environ. 180 (2016) 698–706.
[20] J.A. Seabold, K.S. Choi, J. Am. Chem. Soc. 134 (2012) 2186–2192.
[21] R.L.Z. Hoye, L.C. Lee, R.C. Kurchin, T.N. Huq, K.H.L. Zhang, M. Sponseller, L. Nienhaus, R.E. Brandt, J. Jean, J.A. Polizzotti, A. Kursumović, M.G. Bawendi, V. Bulović, V. Stevanović, T. Buonassisi, J.L. MacManus-Driscoll, Adv. Mater. 2017, 29, 1702176
[22] W. Wei, Y. Dai, B.B. Huang, J. Phys. Chem. C 113 (2009) 5658–5663.
[23] Y. Yang, C. Zhang, C. Lai, G. Zeng, D. Huang, M. Cheng, J. Wang, F. Chen, C. Zhou, W. Xiong, A. Colloid and Interface Sci. 254 (2018) 76–93.
[24] A.H. Lee, Y.C. Wang, C.C. Chen, J. Colloid Interface Sci. 533 (2019) 319–332.
[25] F.Y. Liu, Y.R. Jiang, C.C. Chen, W.W. Lee, Catal. Today 300 (2018) 112–123.
[26] M. Batuk, D. Batuk, A.A. Tsirlin, D.S. Filimonov, Chem. Mater. 27 (2015) 2946–2956.
[27] F.Y. Liu, J.H. Lin, Y.M. Dai, L.W. Chen, S.T. Huang, T.W. Yeh, J.L. Chang, C.C. Chen, Catal. Today 314 (2018) 28–41.
[28] H.P. Lin, W.W. Lee, S.T. Huang, L.W. Chen, T.W. Yeh, J.Y. Fu, C.C. Chen, J. Mol. Catal. A: Chem. 417 (2016) 168–183.
[29] Y. Yu, Y. Gu, W. Zheng, Y. Ding, Y. Cao, J. Phys. Chem. C 119 (2015) 28190–28193.
[30] S. Rau, B. Sc̈hafer, D. Gleich, E. Anders, M. Rudolph, M. Friedrich, H. G̈;orls, W. Henry, J. G. Vos. Angew. Chem. 2006, 118, 6361–6364.
[31] Y. Xia, Z. He, J. Su, Mater. Res. Express 6 (2019) 85909.
[32] S. F̈uldner, P. Pohla, H. Bartling, S. Dankesreiter, R. Stadler, M. Gruber, A. Pfitzner, B. K̈onig, Green Chem. 2011, 13, 640–643.
[33] Y.C. Wang, A.H. Lee, C.C. Chen, J. Taiwan Inst. Chem. E. 93 (2018) 315–328.
[34] B. Wang, J. Di, L. Lu, S. Yan, G. Liu, Y. Ye, H. Lia, W. Zhu, H. Li, J. Xia, Appl. Catal. B. Environ. 254 (2019) 551–559.
[35] B. Wang, G. Liu, B. Ye, Y. Ye, W. Zhu, S. Yin, J. Xia, H. Li, J. Photoch. Photobio. A. 382 (2019) 111901.
[36] Y. Nosaka, A.Y. Nosaka, Chem. Rev. 117 (2017) 11302–11336.
[37] L.S. Zhang, K.H. Wong, H.Y. Yip, C. Hu, J.C. Yu, C.Y. Chan, P.K. Wong, Environ. Sci. Technol. 44 (2010) 1392–1398.
[38] M.C. Yin, Z.S. Li, J.H. Kou, Z.G. Zou, Environ. Sci. Technol. 43 (2009) 8361–8366.
[39] S.G. Meng, D.Z. Li, M. Sun, W.J. Li, J.X. Wang, J. Chen, X.Z. Fu, G.C. Xiao, Catal. Commun. 12 (2011) 972–975.
[40] G. Li, K.H. Wong, X. Zhang, C. Hu, J.C. Yu, R.C.Y. Chan, P.K. Wong, Chemosphere 76 (2009) 1185–1191.
[41] H. Liu, Y. Su, Z. Chen, Z. Jin, Y. Wang, J. Mol. Catal. A: Chem. 391 (2014) 175–182.
[42] M.M. Rahman, K.M. Krishna, T. Soga, T. Jimbo, M. Umeno, J. Phys. Chem. Solid 60 (1999) 201–210.
[43] A.I. Kovalev, D.L. Wainstein, A.Y. Rashkovskiy, A. Osherov, Y. Golan, Surf. Interface Anal. 42 (2010) 850–854.
[44] H.L. Chen, W.W. Lee, W.H. Chung, H.P. Lin, Y.J. Chen, Y.R. Jiang, W.Y. Lin, C.C. Chen, J. Taiwan Inst. Chem. Eng. 45 (2014) 1892–1909.
[45] Y.R. Jiang, H.P. Lin, W.H. Chung, Y.M. Dai, W.Y. Lin, C.C. Chen, J. Hazard. Mater. 283 (2015) 787–805.
[46] D. Chen, H. Feng, J. Li, Chem. Rev. 112 (2012) 6027–6053.
[47] D. Yang, A. Velamakanni, G. Bozoklu, S. Park, M. Stoller, R.D. Piner, S. Stankovich, I. Jung, D.A. Field, C.A. Ventrice, Carbon 47 (2009) 145–152.
[48] L. Lin, S. Yuan, J. Chen, L. Wang, J. Wan, X. Lu, Chemosphere 78 (2010) 66–71.
[49] F. Dong, Y. Sun, M. Fu, Z. Wu, S.C. Lee, J. Hazard. Mater. 219–220 (2012) 26–34.
[50] A. Chatzitakis, C. Berberidou, I. Paspaltsis, G. Kyriakou, T. Sklaviadis, I. Poulios, Water Res. 42 (2008) 386–394.
[51] M. Zubair, H. Kim, A. Razzaq, C. A. Grimes, S. I. In, J. CO2 Util., 2018, 26, 70–79.
[52] A. Razzaq, C.A. Grimes, S.I. In, Carbon 98 (2016) 537–544.
[53] N.M. Dimitrijevic, B.K. Vijayan, O.G. Poluektov, T. Rajh, K.A. Gray, H. He, P. Zapol, J. Am. Chem. Soc. 133 (2011) 3964–3971.
[54] H.Y. Mao, S. Laurent, W. Chen, O. Akhavan, M. Imani, A.A. Ashkarran, M. Mahmoudi, Chem. Rev. 113 (2013) 3407–3424.
[55] Y. Wang, W. Wang, H. Mao, Y. Lu, J. Lu, J. Huang, Z. Ye, B. Lu, ACS Appl. Mater. Interfaces 6 (2014) 12698–12706.
[56] X. Bai, L. Wang, Y. Zhu, ACS Catal. 2 (2012) 2769–2778.
[57] W.W. Lee, C.S. Lu, C.W. Chuang, Y.J. Chen, J.Y. Fu, C.W. Siao, C.C. Chen, RSC Adv. 5 (2015) 23450–23463.
[58] X. Xiao, C. Xing, G. He, X. Zuo, J. Nan, L. Wang, Appl. Catal. B: Environ. 148–149 (2014) 154–163.
[59] H.J. Fan, C.S. Lu, W.L.W. Lee, M.R. Chiou, C.C. Chen, J. Hazard. Mater. 185 (2011) 227–235.
[60] Y.R. Jiang, S.Y. Chou, J. Lin Chang, S.T. Huang, H.P. Lin, C.C. Chen, RSC Adv. 5 (2015) 30851–30860.
[61] W. He, H. Jia, W.G. Wamer, Z. Zheng, P. Li, J.H. Callahan, J.J. Yin, J. Catal. 320 (2014) 97–105.
[62] W. He, H.K. Kim, W.G. Wamer, D. Melka, J.H. Callahan, J.J. Yin, J. Am. Chem. Soc. 136 (2014) 750–757.
[63] M.K. Arfanis, P. Adamou, N.G. Moustakas, T.M. Triantis, A.G. Kontos, P. Falaras, Chem. Eng. J. 310 (2017) 525–536.
[64] K. Li, B.S. Peng, T.Y. Peng, ACS Catal. 6 (2016) 7485–7527.
[65] Z. Sun, J. Melisande T.A. Fischer, Q. Li, J. Hu, Q. Tang, H. Wang, Z. Wu, M. Hankeld, D. J. Searles, L. Wang, Appl. Catal. B: Environ., 2017, 216, 146–155.
[66] H. Zhong, K. Fujii, Y. Nakano, F. Jin, J. Phys. Chem. C 119 (2015) 55–61.